

Retina layer segmentation using kernel graph cuts and continuous max-flow

D. Kaba,^{1,*} Y. Wang,² C. Wang,¹ X. Liu,^{1,3} H. Zhu,^{4,5} A. G. Salazar-Gonzalez,¹ and Y. Li¹

¹Department of Computer Science, Brunel University, UK

²Tongren Hospital, Beijing, China

³Faculty of Engineering, King Abdulaziz University, Jeddah 21589, Saudi Arabia

⁴Department of Optometry and Visual Science, City University, London, UK

⁵National Institute for Health, Research Biomedical Research, Centre at Moorefields, Eye Hospital NHS Foundation, Trust and UCL Institute of Ophthalmology, London, UK

*yongmin.li@brunel.ac.uk

Abstract: Circular scan Spectral-Domain Optic Coherence Tomography imaging (SD-OCT) is one of the best tools for diagnosis of retinal diseases. This technique provides more comprehensive detail of the retinal morphology and layers around the optic disc nerve head (ONH). Since manual labelling of the retinal layers can be tedious and time consuming, accurate and robust automated segmentation methods are needed to provide the thickness evaluation of these layers in retinal disorder assessments such as glaucoma. The proposed method serves this purpose by performing the segmentation of retinal layers boundaries in circular SD-OCT scans acquired around the ONH. The layers are detected by adapting a graph cut segmentation technique that includes a kernel-induced space and a continuous multiplier based max-flow algorithm. Results from scan images acquired with Spectralis (Heidelberg Engineering, Germany) prove that the proposed method is robust and efficient in detecting the retinal layers boundaries in images. With a mean root-mean-square error (RMSE) of 0.0835 ± 0.0495 and an average Dice coefficient of 0.9468 ± 0.0705 pixels for the retinal nerve fibre layer thickness, the proposed method demonstrated effective agreement with manual annotations.

© 2015 Optical Society of America

OCIS codes: (100.2960) Image analysis; (100.2980) Image enhancement; (110.4500) Optical coherence tomography; (170.2960) Medical and biological imaging.

References and links

1. D. Huang, E. A. Swanson, C. P. Lin, J. S. Schuman, W. G. Stinson, W. Chang, M. R. Hee, T. Flotte, K. Gregory and C. A. Puliafito, "Optical coherence tomography," *Science* **254**(5035), 1178–1181 (1991).
2. J. S. Schuman, M. R. Hee, A. V. Arya, T. Pedut-Kloizman, C. A. Puliafito, J. G. Fujimoto and E. A. Swanson, "Optical coherence tomography: a new tool for glaucoma diagnosis," *Current opinion in ophthalmology* **6**(2), 89–95 (1995).
3. V. Guedes, J. S. Schuman, E. Hertzmark, G. Wollstein, A. Correnti, R. Mancini, D. Lederer, S. Voskianian, L. Velazquez and H. M. Pakter, "Optical coherence tomography measurement of macular and nerve fiber layer thickness in normal and glaucomatous human eyes," *Ophthalmology* **110**, 177–189 (2003).
4. A. F. Fercher, C. K. Hitzenberger, G. Kamp and S. Y. El-Zaiat, "Measurement of intraocular distances by back-scattering spectral interferometry," *Optics Communications* **117**, 43–48 (1995).
5. M. Wojtkowski, R. Leitgeb, A. Kowalczyk, A. F. Fercher and T. Bajraszewski, "In vivo human retinal imaging by Fourier domain optical coherence tomography," *Journal of biomedical optics* **7**(3), 457–463 (2002).

6. D. Koozekanani, K. Boyer and C. Roberts, "Retinal thickness measurements from optical coherence tomography using a Markov boundary model," *Medical Imaging, IEEE Transactions (IEEE 2001)* **20**(9), 900–916.
7. H. Ishikawa, D. M. Stein, G. Wollstein, S. Beaton, J. G. Fujimoto and J. S. Schuman, "Macular segmentation with optical coherence tomography," *Investigative Ophthalmology & Visual Science* **46**(6), 2012–2017 (2005).
8. D. Cabrera Fernández, H. M. Salinas and C. A. Puliafito, "Automated detection of retinal layer structures on optical coherence tomography images," *Optics Express* **13**(25), 10200–10216 (2005).
9. C. Ahlers, C. Simader, W. Geitzenauer, G. Stock, P. Stetson, S. Dastmalchi and U. Schmidt-Erfurth, "Automatic segmentation in three-dimensional analysis of fibrovascular pigmentepithelial detachment using high-definition optical coherence tomography," *British Journal of Ophthalmology* **92**(2), 197–203 (2008).
10. M. Mujat, R. Chan, B. Cense, B. Park, C. Joo, T. Akkin, T. Chen and J. de Boer, "Retinal nerve fiber layer thickness map determined from optical coherence tomography images," *Optics Express* **13**(23), 9480–9491 (2005).
11. A. Yazdanpanah, G. Hamarneh, B. R. Smith and M. V. Sarunic, "Segmentation of intra-retinal layers from optical coherence tomography images using an active contour approach," *Medical Imaging, IEEE Transactions on (IEEE 2011)* **30**(2), 484–496.
12. J. Novosel, K. A. Vermeer, G. Thepass, H. G. Lemij and L. J. van Vliet, "Loosely coupled level sets for retinal layer segmentation in optical coherence tomography," In *Biomedical Imaging (ISBI), 2013 IEEE 10th International Symposium on 2013*, 1010–1013.
13. H. Zhu, D. P. Crabb, P. G. Schlottmann, T. Ho and D. F. Garway-Heath, "FloatingCanvas: quantification of 3D retinal structures from spectral-domain optical coherence tomography," *Optics express* **18**(24), 24595–24610 (2010).
14. M. K. Garvin, M. D. Abràmoff, R. Kardon, S. R. Russell, X. Wu and M. Sonka, "Intraretinal layer segmentation of macular optical coherence tomography images using optimal 3-D graph search," *Medical Imaging, IEEE Transactions on 2008* **27**(10), 1495–1505.
15. M. K. Garvin, M. D. Abràmoff, X. Wu, S. R. Russell, T. L. Burns and M. Sonka, "Automated 3-D intraretinal layer segmentation of macular spectral-domain optical coherence tomography images," *Medical Imaging, IEEE Transactions on 2009* **28**(9), 1436–1447.
16. S. J. Chiu, X. T. Li, P. Nicholas, C. A. Toth, J. A. Izatt and S. Farsiu, "Automatic segmentation of seven retinal layers in SDOCT images congruent with expert manual segmentation," *Optics express* **18**(18), 19413–19428 (2010).
17. O. S. Anthony, "Is Imaging Now Standard of Care for Glaucoma?" <http://www.revoptom.com/content/c/19985>.
18. N. j. Tustison, B. B. Avants, P. A. Cook, Y. Zheng, A. Egan, P. A. Yushkevich and J. C. Gee, "N4ITK: improved N3 bias correction," *Medical Imaging, IEEE Transactions on 2010* **29**(6), 1310–1320.
19. M. B. Salah, A. Mitiche and I. B. Ayed, "Multiregion image segmentation by parametric kernel graph cuts," *Image Processing, IEEE Transactions on 2011* **20**(2), 545–557.
20. J. Yuan, E. Bae and X. C. Tai, "A study on continuous max-flow and min-cut approaches," In *Computer Vision and Pattern Recognition (CVPR), 2010 IEEE Conference on IEEE 2010*, 2217–2224.
21. J. G. Sled, A. P. Zijdenbos and A. C. Evans, "A nonparametric method for automatic correction of intensity nonuniformity in MRI data," *Medical Imaging, IEEE Transactions on 1998* **17**, 87–97.
22. Y. Y. Boykov and M. P. Jolly, "Interactive graph cuts for optimal boundary & region segmentation of objects in ND images," In *Computer Vision, 2001. ICCV 2001. Proceedings. Eighth IEEE International Conference on, Volume 1 IEEE 2001*, 105–112.
23. R. A. Costa, M. Skaf, L. A. Melo Jr, D. Calucci, J. A. Cardillo, J. C. Castro, D. Huang and M. Wojtkowski, "Retinal assessment using optical coherence tomography," *Progress in retinal and eye research* **25**(3), 325–353 (2006).
24. A. Lang, A. Carass, E. Sotirchos, P. Calabresi and J. L. Prince, "Segmentation of retinal OCT images using a random forest classifier," In *SPIE Medical Imaging, International Society for Optics and Photonics, 86690R–86690R (2013)*.

1. Introduction

Optical coherence tomography (OCT) imaging has been largely used in ophthalmology as a tool for assessing and monitoring morphological features such as the thickness of the retinal layers [1]. The time-domain OCT is one of the first OCT imaging techniques in retinal diseases diagnosis [2, 3]. However this technique has its limitations. The time domain OCT can only provide the RNFL thickness measurements in a line scan.

To address these limitations, the Spectral-Domain Optic Coherence Tomography SD-OCT [4, 5] was developed with faster scan capability that provides the most comprehensive structure of the retina. With these new capabilities, this imaging equipment possesses a powerful tool that allows a 3-D image of the retina to be formed in routine clinical scans. The SD-OCT generates

an image by an in-depth axial scan known as an A-scan. A series of successive A-scans form a cross sectional 2-D image known as a B-scan. Using a series of successive B-scans, a 3-D image volume of the retina is yielded. This new technique is used in modern ophthalmology to assist the diagnosis of retinal diseases such as glaucoma, diabetic retinopathy, neo-vascularisation, vein occlusion and many more vision impairment diseases.

The evaluation of the RNFL thickness in glaucomatous damage requires segmentation of different retinal layers. This process can be time consuming and tedious when it is done by hand. Therefore there is a need for a robust and reliable automated segmentation algorithm in computer-aided diagnosis, which preserves various retinal layer shapes.

Circular scan SD-OCT imaging has become one of the best tools for diagnosis of retinal diseases. This technique provides a more comprehensive detail of the retinal morphology and layers around the optic disc nerve head (ONH). However accurate automated segmentation methods are needed to provide the thickness evaluation of these layers, since manually labelling these retinal layers can be tedious and time consuming.

Recently many methods for retinal layers segmentation in the OCT image have been extensively studied. Early methods were purely based on pixel intensity variation (high and low tissue reflectivity) processing operations along A-scan profile [6–9]. These methods detected the retinal layer boundary by setting a target threshold value for the layer tissue pixel intensity. They are computationally efficient, but often suffer because of the variation of intensity within layers. This inconsistency of intensity is commonly generated by the blood vessels artefacts (shadows) during the OCT imaging. Some other segmentation techniques use image gradients, prior layer shape information and many other constraints to perform the segmentation of the layers. Some of these segmentation technique are active contours, graph cut and machine learning approaches. The active contours segmentation technique uses an energy formulation consisting of gradient, edge density and boundary smoothness. In [10], Mujat et al performed the segmentation of the RNFL thickness in SD-OCT image using anisotropic noise suppression operation and deformable splines. This technique is not affected by any intensity variation but it is sensitive to the artefacts of the blood vessels in the OCT image. Yazdanpanah et al [11], used Chan-Vese energy-minimising active contours to segment the intra-retinal layers by incorporating a circular shape in order to model the boundaries of retinal layers. This method is also less affected by the intensity variations, however the constraints on the boundaries can lead to errors when segmenting irregular layer shapes. In [12], Novosel et al utilised Bayesian inference in level sets to segment three retinal layers in SD-OCT retinal image. All the layers are simultaneously detected using prior knowledge of the layers. This segmentation approach is also sensitive to the blood vessel artefacts. Zhu et al [13] provided a FloatingCanvas technique for retinal layer segmentation in 3-D SD-OCT. The algorithm makes use of analytical surface deformable and prior information about the layers location in the OCT image. This method is sensitive to low gradient on the region of the vitreous-RNFL boundary of some OCT images. Garvin et al [14] segmented five retinal layers in 3-D SD-OCT by finding a minimum-cost in a geometric graph formulated from edge information and priori surface information. This technique was improved in [15], which simultaneously segmented retinal layers by learning the cost function and constraints from a training set and by using a 3-D graph search technique. The graph search method was extended in [16] by Chiu et al, to segment eight retinal layer boundaries on individual B-scan in the SD-OCT using dynamic programming.

The majority of these methods [10–13] and [15, 16] used prior knowledge about the layers to apply constraints such as shapes and positions on the segmentation algorithms. These constraints can lead to segmentation errors when the algorithms are used on irregular retinal layers or new OCT data sets. Also the graph-based segmentation methods have problems in finding appropriate cost functions on the graph formulation to distinguish individual layers.

Another issues with the graph-based segmentation is the efficiency of the optimisation operations to accurately detect the layers boundaries. Furthermore, segmentation algorithms used in many commercially available OCT imaging tools encounter enormous problems segmenting the RNFL layers in OCT images with poor scanning quality or noise as seen in Fig. 1 [17].

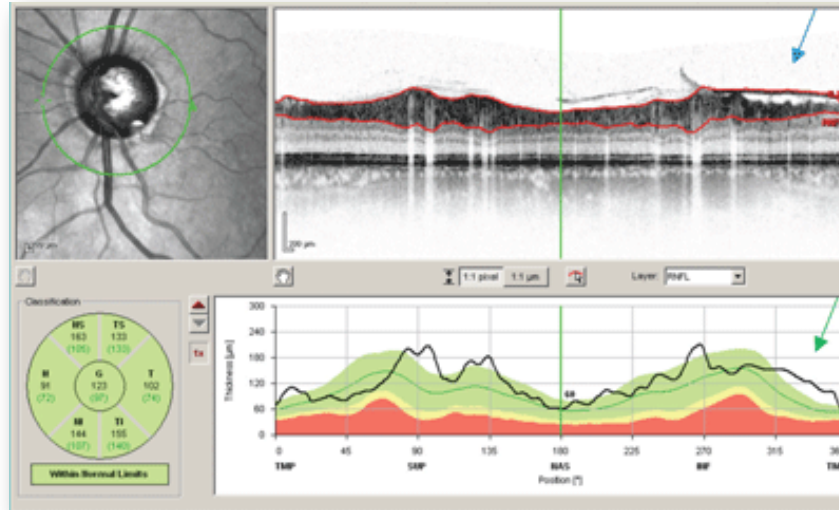


Fig. 1. Error in measuring the RNFL thickness. Top left: circular scan. Top right: error in segmentation line at the inferior temporal quadrant indicated by the blue arrow caused by poor scan quality. Bottom right: the inferior temporal RNFL thickness is measured as abnormal shown by the green arrow. Bottom left: The classification chart showing the overall results of the RNFL thickness measurement within normal boundaries. [17].

The aim of this work is to develop a new automated segmentation method to address the limitations of the existing for the RNF detection. It also provides a good balance between efficiency and robustness. Our method addresses some these segmentation problems using the bias correction algorithm [18] to eliminate the image artefacts and a graph cut based segmentation technique which incorporates the mechanism of the kernel induced function [19] and a continuous Max-flow to allow better detection of retinal layers. The proposed method also addresses the layers detection problem in the presence noises reports in [17].

Because of the above advantages, our method performs better than the previous methods. In particular for difficult cases. We tested our method on 120 SD-OCT circular scans around the ONH. All the images were acquired with SD-OCT Spectralis HRA + OCT (Heidelberg Engineering, Germany). We believe our method would perform well on OCT images with diseases such as exudates, haemorrhage, swelling, edema, cyst, detachment, epimembrane, because the nature of the problems is similar, although we do not have access to these types of data currently. Figure 2 shows the different images of the retina in the circular scan.

2. Methods

In this study, the segmentation of retinal layers boundaries including the vitreous-retinal nerve fiber layer (RNFL) or inner limiting membrane (ILM), RNFL-ganglion cell layer (RNFL-GCL) and the retinal pigment epithelium (RPE) was performed. The segmentation method starts by removing some common medical imaging artefacts from the retinal SD-OTC circular images

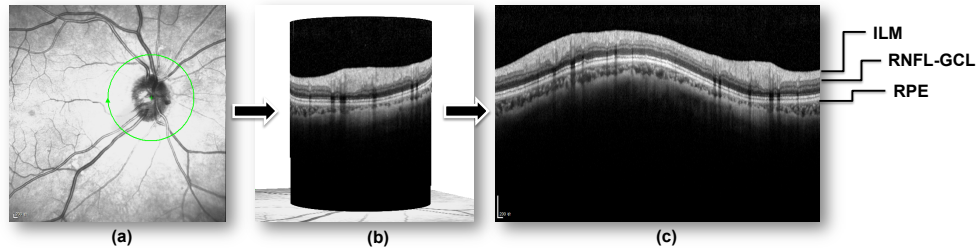


Fig. 2. D-OCT circular imaging process. (a) Circular scan on the OCT fundus image, (b) Retinal tissues (Layers) image from the scan, (c) A 2-D OCT cross-sectional image of the layers tissues.

such as intensity inhomogeneity and noise. This operation is performed using the bias correction technique [18] and it is expected to improve the robustness of the retinal tissue layers segmentation. The boundaries of the ILM, RNFL-GCL and RPE are detected by adapting a multiregional graph cut segmentation technique [19], that includes a kernel induced segmentation functional and a continuous multiplier based max-flow algorithm [20]. Figure 3 shows the illustration of the segmentation method.

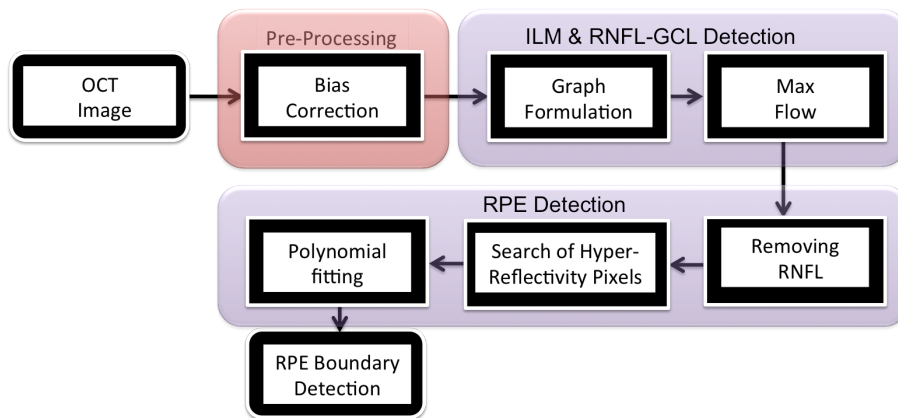


Fig. 3. Algorithm of the segmentation method.

2.1. Bias correction

The boundaries of retinal layers are not well defined in the SD-OCT circular scans due to the noises and intensity inhomogeneity in the images. The bias correction algorithm [18] is used to correct the intensity inhomogeneity and remove noise from the image. This algorithm corrects the imaging artefacts by estimating the residual bias field which is then subtract from the corrupted image to provide an enhance image. This pre-processing operation enhances the boundaries of the layers, which reduce false positives during the segmentation process. Figure 4 shows the results of the bias correction operation, where Fig. 4(c) is the corrected image with well-defined layers boundaries.

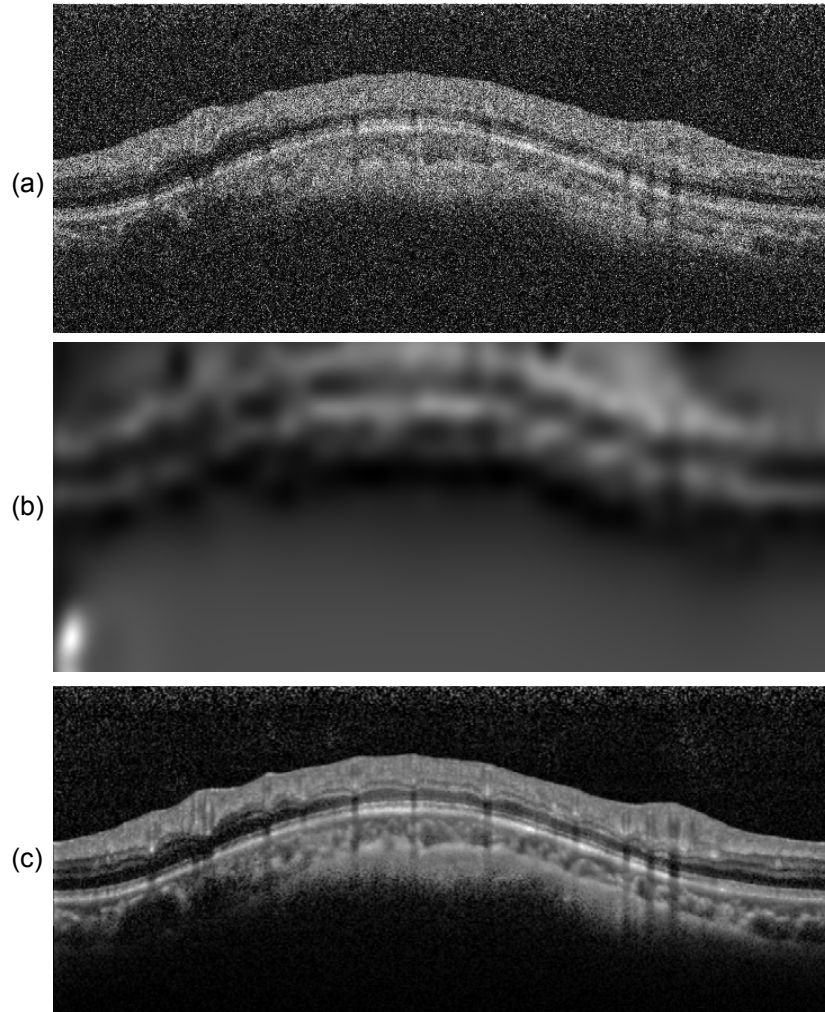


Fig. 4. Pre-processing. (a) SD-OCT circular scan image. (b) Bias image. (c) Bias corrected image.

2.2. Graph construction for the detection of ILM and RNFL-GCL boundaries

To perform the segmentation of the ILM and RNFL-GCL boundaries, we represent each circular B-scan image as a graph $G(v, \epsilon)$ consisting of a set of vertex or nodes (pixels) v and a set of directed edges ϵ connecting neighbouring pixels. In the circular B-scan image nested grid, the graph contained two special terminal nodes, a foreground terminal (source s) in our case the ILM and RNFL-GCL pixels and a background terminal (sink t). The edge set ϵ includes the (n-links) linking two neighbourhood nodes in the image grid and the terminal links or data edge (s-links and t-links) connecting the source s and sink t to each node in the image grid respectively. Each pixel $p \in \Omega$ (a set of pixels) in the grid is connected to the terminals by s-links with $\{p, s\}$ and t-links with $\{p, t\}$ while a pair of neighbouring pixels $\{p, q\} \in N$ (number of pixel neighbour) is connected by n-links [22]. The set of connected edges provides a pathway through which one can travel across the graph. The path preferences are created by assigning non-negative weight (cost) $W_e > 0$ to each edge $e \in \epsilon$. To obtain good segmentation

results of the boundaries, the preferred path should have the minimum total weights of edges for travelling from a start node to an end node of the graph. The resulting path from this operation represents the cut, which separates the image into two disjoint partitions, including ILM + RNFL-GCL layer and the background.

If we denote s-t the cut that separates the image into two disjoint partitions, this cut can be defined by a subset of edges $C \in \varepsilon$ where $G(c) = \langle v, \varepsilon \setminus C \rangle$. C is defined as $|C| = \sum_{e \in C} W_e$. C cuts the graph into two separate regions as defined in the equation below.

$$\varepsilon = F_g \cup B_g, F_s \cap B_t = \emptyset \quad (1)$$

F_g are pixels labelled as foreground (ILM, RNFL-GCL boundaries) while B_g are the pixels mapped as background. Figure 5 shows an example of graph construction where the red and blue dots represent the pixels grid. The solid red lines show a strong connection of red pixels to the foreground (pixels belong to foreground) and the thin red lines represent a weak connection between the blue pixels and the foreground pixels. The solid blue lines also represent a strong connection between the blue pixels and the background pixels whereas the thin lines show weak connection between the red and background pixels.

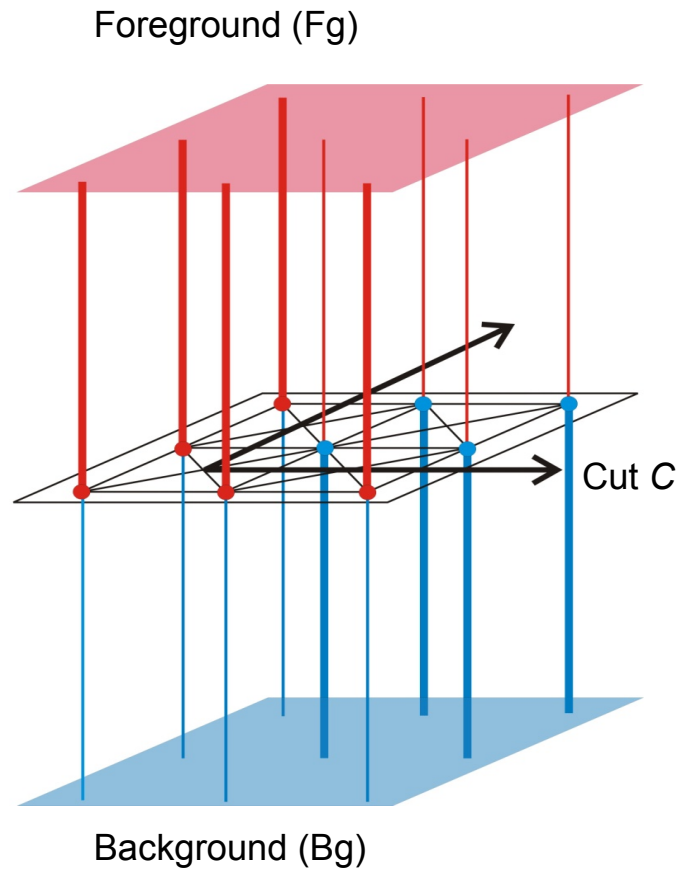


Fig. 5. Graph illustration. Example of graph construction

To define the segmentation functional of the graph, let us assume a binary labelling set $A = (A_1, A_p, \dots, A_p)$, which is assigned to each pixel $p \in \Omega$ in the circular image grid and let A_p

indicate assignment to pixels $p \in \Omega$. Each assignment A_p in the circular image grid is either in the foreground Fg (ILM, RNFL-GCL) boundaries or background (Bg). Thus the segmentation functional can be defined as:

$$E(A) = \lambda \cdot R(A) + B(A). \quad (2)$$

where $R(A)$ is the data term (regional term) that measures the similarity between neighbouring pixels in a circular image Ω . $B(A)$ is the prior (boundary term), for smoothing regions boundaries and λ a positive coefficient indicating the relative importance of the regional term against the boundary term. The regional (the likelihood of the foreground and background) can then be written as:

$$R(A) = \sum_{p \in \Omega} R_p(A_p) = \sum_{A_p \in A} \sum_{p \in S_{A_p}} -\log(I_p/S_{A_p}). \quad (3)$$

where S_{A_p} is the image region whose label is A_p and (I_p/S_{A_p}) is the conditional probability of a pixel in data grid (I_p) given a model distributions within each image region. If κ_{A_p} is the piecewise constant model parameter of image region or image region parameter S_{A_p} , the data term (3) can be expressed as:

$$R(A) = \sum_{p \in \Omega} R_p(A_p) = \sum_{A_p \in A} \sum_{p \in S_{A_p}} (\kappa_{A_p} - I_p)^2. \quad (4)$$

The boundary term is expressed as follows:

$$B(A) = \sum_{p,q \in N} B_{p,q} \cdot \phi(A_p, A_q) \quad (5)$$

For $A_p \neq A_q$

$$\phi(A_p, A_q) = 1$$

$$\phi(A_p, A_q) = 0 \text{ Otherwise}$$

$$B_{p,q} = \exp\left(-\frac{(I_p - I_q)^2}{2\sigma^2}\right) \cdot \frac{1}{\text{dist}(p, q)} \quad (6)$$

where $R_p(A_p)$ assigns pixel p to either ILM, RNFL-GCL boundaries (Fg) or the background (Bg). $B_{p,q}$ indicates the discontinuity between neighbouring pixels. The value of $B_{p,q}$ is large when I_p and I_q are similar and it is close to zero when I_p and I_q are different.

The data term of the graph formulation is defined by first transforming the image data implicitly using a kernel function where the piecewise constant model of the graph cut formulation is applicable. This operation allows a better partition of a non-linearly separable data [19]. Introducing the kernel function into the graph energy formulation gives a kernel induced segmentation function [19] as:

$$E(\{\kappa_{A_p}\}, A_p) = \sum_{A_p \in A} \sum_{p \in S_{A_p}} D_F(I_p, \kappa_{A_p}) + \lambda \sum_{p,q \in N} B_{p,q} \cdot \phi(A_p, A_q). \quad (7)$$

The kernel induced segmentation functional expressed in (7) depends on the labelling function A and the image region parameter κ_{A_p} .

In our implementation, we use the Radial basis function kernel (RBF), which is defined by:

$$F(Y, Z) = \exp\left(-\frac{\|Y - Z\|^2}{\sigma^2}\right). \quad (8)$$

The functional in (7) is optimised using a continuous multiplier based max-flow algorithm [20]. The multiplier based max-flow algorithm is used because it splits the optimisation problem into simple sub problems over independent flow variables and is globally optimised. This optimisation operation separates the circular image into retinal RNFL boundaries (ILM+RNFL-GCL) and the photoreceptor layer that includes the RPE layer. Figure 6 shows the segmentation results of the proposed method of ILM and RNFL-GCL boundaries.

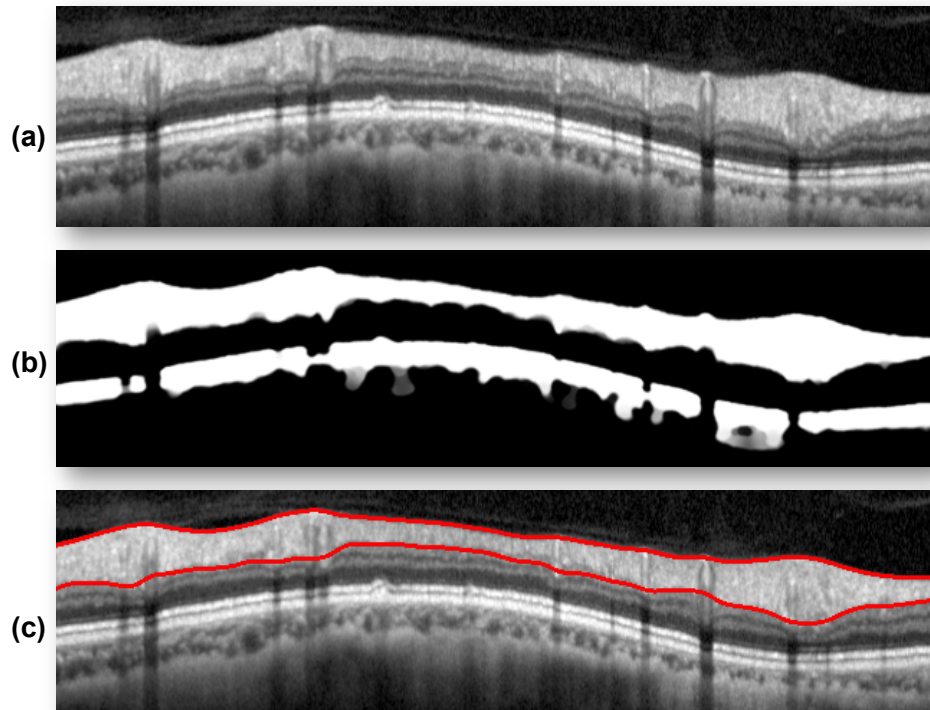


Fig. 6. ILM and RNFL-GCL boundaries detection. (a) Circular scan image, (b) Segmented binary image, (c) ILM and RNFL-GCL boundaries in red.

2.3. Detection of the RPE layer boundaries

The RPE layer detection is performed using prior knowledge about the SD-OCT image and its features. Based on clinical and tomographical correlation studies [23], it had been suggested that the RPE-choriocapillaris layer exhibits the most hyper-reflectivity layer in the retinal SD-OCT imaging. While the RNFL represents some of the hyper-reflectivity pixels at the top of the retinal SD-OCT image as seen in Fig. 7(a).

To segment the RPE layer, we first perform the search for all the hyper-reflectivity pixels (highest intensity values) in circular scan image. These pixels correspond to the most reflective layer (RPE). However to prevent the algorithm from selecting hyper-reflectivity pixels in the RNFL that also exhibit some bright pixels, it is helpful to constrain the search to a region of interest (RPE layer). The boundaries of the RNFL is already accurately detected in Section (2.2), thus we may set all pixels belonging to the RNFL to zero before searching for the hyper-reflectivity pixels. By setting the RNFL pixels to zero, the search area of the bright pixels is limited to the space shown in Fig. 7(b).

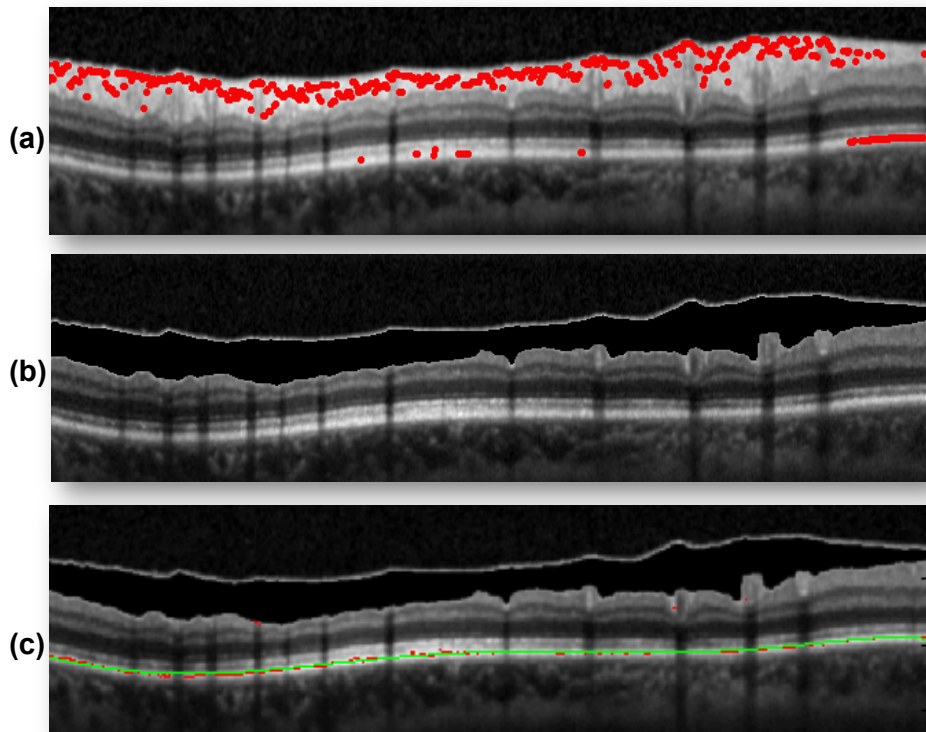


Fig. 7. RPE boundary detection. (a) Hyper-reflectivity pixels in red on RNFL layer , (b) Selection of region of interest, (c) RPE boundary in green.

After the selection of all the hyper-reflectivity points in the region of interest, a polynomial curve fitting process is used to construct a curve that has the best fit to the series of hyper-reflectivity pixels. The degree of the polynomial curve in our case was set to 6. Results of the segmentation of the RPE using the polynomial curve fitting are shown in Fig. 7(c).

3. Experiments

The data used in this study was obtained from on going research on the prevention of retinal disease such as glaucomatous damage, diabetic retinopathy, age-related conditions, optic neuropathy, macular degeneration or other significant retina diseases in Tongren Eye Hospital. 120 SD-OCT circular scans around ONH were obtained from patients with an age range of 20-85 years. A scans of both eyes of each patient was acquired with a high-resolution SD-OCT Spectralis HRA+OCT (Heidelberg Engineering, Germany). The SD-OCT imaging of the optic nerve was performed using a scan protocol that applies a circle of diameter 3.4 mm centred on the ONH. Figure 2 shows the scan process of the retinal optic nerve. In Fig. 2(a) a green circular scanning path of diameter 3.4 mm centred on the ONH of OCT fundus image is used to capture a scan of the retinal layers tissues as seen in Fig.2(b). Figure 2(c) transformation of the circular scan into a 2-D OCT cross-sectional image (B-scan) of the layers tissues with different layers boundaries definitions. The proposed method is implemented on MATLAB R2011b and the computation time of our algorithm is less than 70 seconds for an OCT scan image on a MAC OX X running at 2.66 GHz, with 4G of RAM memory.

3.1. Segmentation accuracy

In this study three retinal boundaries were evaluated including ILM, peripapillary RNFL-GCL and the RPE as well as the thickness of the RNFL. The measurement of these boundaries plays an important role in the application of the OCT imaging in diagnose and prevention of retinal disease such as glaucomatous damage.

To evaluate accurately the segmentation of the ILM, RNFL-GCL and the RPE boundaries by the proposed method, the results of the segmentation were compared to the manual annotations of the ILM, RNFL-GCL and the RPE in the circular scans. The mean absolute deviation (MAD), the root-mean-square (RMSE) and the dice coefficient were used to evaluate the method on the ILM, RNFL-GCL and the RPE against the corresponding manually labelled image. The MAD, RMSE and the Dice coefficient are computed as follow:

$$\begin{aligned} \text{MAD}(\text{GT}, \text{SEG}) &= 0.5 * \left(\frac{1}{n} \sum_{i=1}^n d(pt_i, \text{SEG}) + \frac{1}{m} \sum_{i=1}^m d(ps_i, \text{GT}) \right) \\ \text{RMSE} &= \sqrt{\frac{1}{n} \sum_{i=1}^n (\text{SEG}_i - \text{GT}_i)^2} \\ \text{Dice} &= \frac{2|\text{GT}_i \cap \text{SEG}_i|}{|\text{GT}_i| + |\text{SEG}_i|} \end{aligned} \quad (9)$$

where SEG_i is the pixel labelled as retinal Layer by the proposed segmentation method and GT_i is the true retinal layers pixel in the manual annotation image. pt_i and ps_i represent the coordinates of the images, $d(pt_i, \text{SEG})$ is the distance of pt_i to the closest pixel on SEG with the same segmentation label, $d(ps_i, \text{GT})$ is the distance of ps_i to the closest pixel on GT with the same segmentation label, n and m are the number of points on SEG) and GT respectively.

In addition, further evaluation was conducted on the area between the anterior (ILM) and posterior (RNFL-GCL) boundaries of the RNFL (RNFL thickness) using the following evaluation measurement.

Table 1. Performance evaluation with RMSE (Standard deviation) and MAD (Standard deviation) for each boundary. The values have units of pixels. - 120 OCT Scans.

All Images	Mean RMSE	Mean MAD
ILM	0.0453(0.0276)	0.3931(0.2905)
RNFL-GCL	0.0582(0.0329)	1.2785(1.0523)
RPE	0.0124(0.0124)	0.2131(0.3108)

$$\begin{aligned} \text{TPR} &= \frac{\text{TP}}{\text{GT}_{\text{RNFL pixels}}} \\ \text{FPR} &= \frac{\text{FP}}{\text{GT}_{\text{Non RNFL pixels}}} \end{aligned} \quad (10)$$

where TP is the true positive, FP is the false positive and $\text{GT}_{\text{RNFL pixels}}$ and $\text{GT}_{\text{Non RNFL pixels}}$ represent the manually labelled RNFL layer pixels and non RNFL pixels in the image. Also TPR, FPR are the true positive rate (sensitivity) and the false positive rate.

Table 1 shows the evaluation of the proposed method on 120 OCT scans including 100 healthy and 20 diseased retinas. The RPE boundary detection of all the 120 images with mean

Table 2. **Performance comparison of healthy versus disease images.** -OCT Scans.

Heathy images	Mean RMSE	Mean MAD
ILM	0.0474(0.0286)	0.4166(0.3023)
RNFL-GCL	0.0610(0.0312)	1.3835(1.0683)
RPE	0.0103(0.0084)	0.1504(0.2565)
Unhealthy images	Mean RMSE	Mean MAD
ILM	0.0346(0.0198)	0.2753(0.1867)
RNFL-GCL	0.0440(0.0382)	0.7536(0.8002)
RPE	0.0072(0.0129)	0.1379(0.2814)

RMSE = 0.0124 ± 0.0124 and MAD = 0.2131 ± 0.3108 has the lowest boundary error against the other layers boundaries (ILM and RNFL-GCL). The algorithm achieves a high performance on the RPE boundary detection because it segments the boundary using polynomial fitting as well as removing all the other hyper-reflectivity pixels in the image. While in the literature, the RPE boundary is considered as the most difficult boundary to detect since it has the most hyper-reflectivity pixels and it is not always visible through all OCT images as it has tendency to appear and disappear [24]. This phenomenon is due to the blood vessels artefacts (shadows) in the OCT retina image.

The ILM boundary detection also has a very low boundary error with mean values of RMSE = 0.0453 ± 0.0276 and MAD = 0.3931 ± 0.2905 . This low error is expected because the ILM boundary is the location where the retinal tissue layer in the OCT image has a large gradient, as it is the area where the background and retina tissue intersected. However the RNFL-GCL boundary has also low mean RMSE = 0.0582 ± 0.0329 and reasonable high MAD = 1.2785 ± 1.0523 . This large error is caused by the presence of the blood vessels shadows on the RNFL-GCL boundary, while manual segmentation ignore the vessels artefacts. Including these areas of the vessels in the automated segmentation can also led to some error in assessing the retinal layer thickness. Figure 8(b) shows the segmentation results of the RNFL-GCL boundary with some blood vessels artefacts indicated with blue arrays.

Table 2 shows the evaluation of the proposed method on healthy and diseased retina including 100 healthy and 20 diseased images. Similar to Table 1, in Table 2 the RPE boundary achieved the best overall segmentation value in both healthy and diseased images followed by the ILM boundary. The proposed method performed well on both healthy and diseased images.

Table 3 shows the values of the TPR, FPT and Dice coefficient of the performance evaluation between the estimated RNFL thickness and the true RNFL thickness. With the value of TPR = 97.46%, our method achieves very good segmentation results and its comparable to the results of the manual segmentation. However the value of the FPR = 8.67% is slightly higher, this is largely due again to the blood vessels artefacts around the RNFL-GCL boundary, where the vessels appear as false positive. To solve this problem [12] included the blood vessels areas in the OCT image from the accuracy evaluation to improve the segmentation errors. Considering the value of the Dice coefficient Dice = 0.9468 ± 0.0705 , RMSE = 0.0835 ± 0.0495 as performance measures, the proposed method performs well for the segmentation of the RNFL thickness. Similar to the results in Table 1 and Table 2, Table 3 also shows higher performance of the proposed method on pathological retina with TPR = 98.59% and FPR = 5.57%. These results are due to the large gradient on the region of the ILM boundary and the thin RNF in diseased retina. We have also performed a confidence interval analysis for the estimated TPR, FPR, Dice and RMSE. The confidence intervals for these measures at the 95% confidence level are provided in the last column of Table 3. Figure 9 shows the comparison of the proposed segmentation results on the ILM, RNFL-GCL and RPE boundaries and the Human manual grading

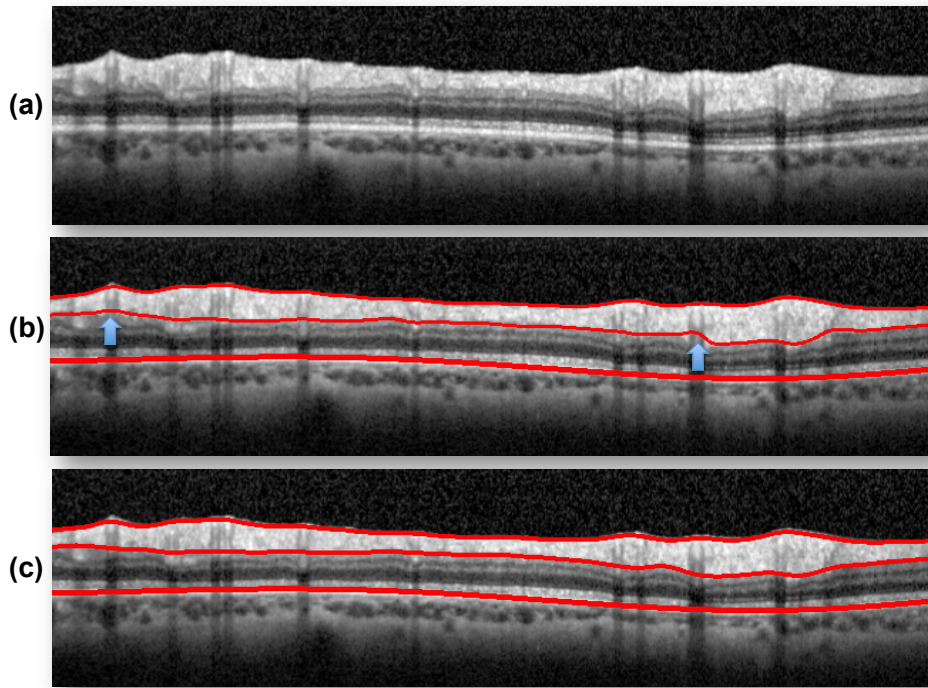


Fig. 8. Results. (a) Circular scan , (b) Segmentation result of the proposed method, (c) Human manual grading image.

images.

Table 3. Performance evaluation of TPR, FPR, Dice coefficient and RMSE, Standard deviation (Std) and the 95% Confidence interval between the estimated RNFL thickness and the true RNFL thickness -OCT Scans.

Images	RNFLT	std	conf
Mean TPR	0.9746	0.0665	± 0.0119
Mean FPR	0.0867	0.1037	± 0.0186
Mean Dice	0.9468	0.0705	± 0.0126
Mean RMSE	0.0835	0.0495	± 0.0089
Heathy images			
Mean TPR	0.9792	0.0230	± 0.0045
Mean FPR	0.0919	0.0947	± 0.0186
Mean Dice	0.9473	0.0404	± 0.0079
Mean RMSE	0.0881	0.0418	± 0.0082
Unhealthy images			
Mean TPR	0.9859	0.0215	± 0.0042
Mean FPR	0.0557	0.0970	± 0.0190
Mean Dice	0.9676	0.0401	± 0.0079
Mean RMSE	0.0586	0.0521	± 0.01021

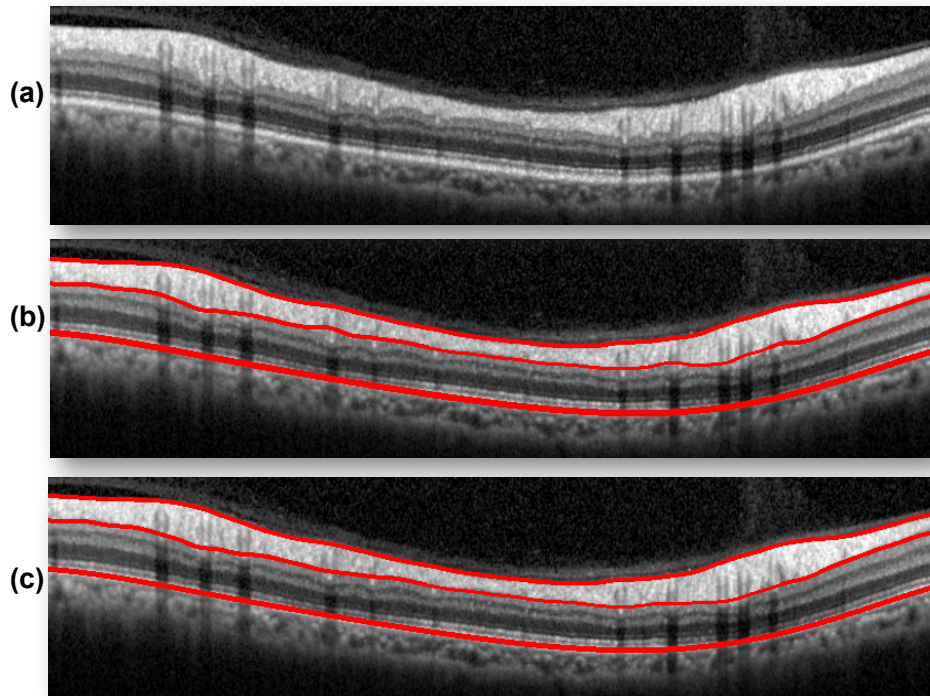


Fig. 9. Results. (a) Circular scan image, (b) Segmentation result of the proposed method, (c) Human manual grading image.

3.2. RNFL thickness profiles

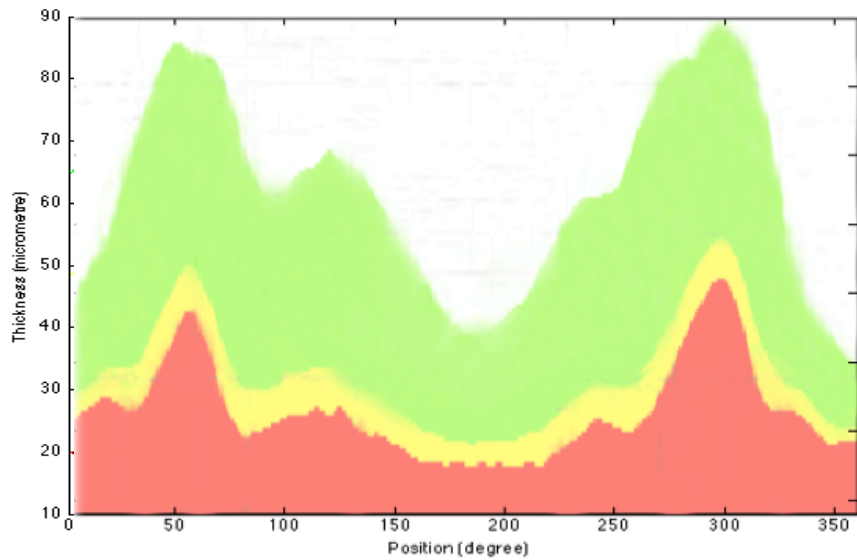
In addition to the evaluation of the RNFL thickness, we provided the RNFL thickness profile graph. The thickness profile graph provides the following information:

- The RNFL thickness profile measured along the circular scan of the retina;
- The RNFL thickness profile of the normative database, allowing the comparison of our segmentation thickness values to the normal range.

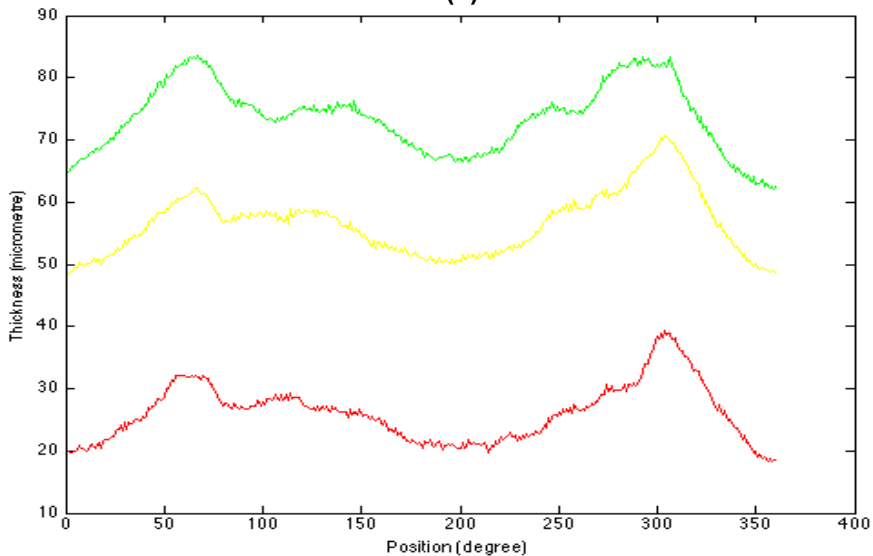
This thickness profile graph is obtained from a normative database compiled by Spectralis HRA+OCT (Heidelberg Engineering GmbH, Germany). Figure 10 shows the thickness profile graph, where the x-axis indicates the length of the circular scan (position in degree) and the y-axis displays the RNFL thickness in pixels. The colour coding the thickness profile graph indicate whether a given retina thickness is within normal limits (green), outside the normal limits (red) or on the border of normal limits (yellow). The green region represents the mean RNFL thickness of healthy eyes.

The 1 – 5% range is used to estimate the risky profile (shown as yellow in the figures), while the diseases profile is actually constructed from the much smaller < 1% range. These parameters can be easily adjusted in our implementation, and we are willing to accept any advices from the reviewer and other experts on this to generate better profile models.

We selected the range of the RNFL thickness profile from the Spectralis HRA+OCT user manual software version 5.7. The healthy eyes (normal limits or green) is indicated by the



(a)



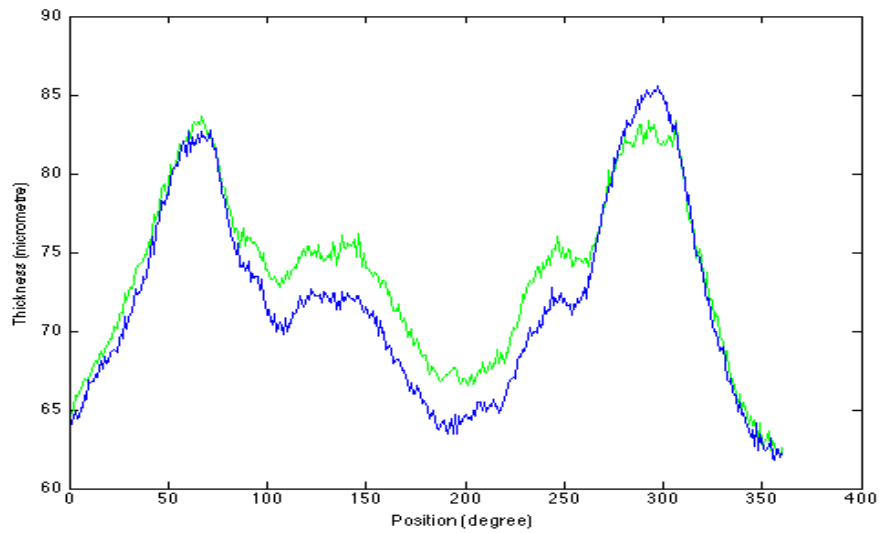
(b)

Fig. 10. Results(Top: Normative database of retinal RNFL thickness. Bottom: Proposed method RNFL thickness profile. (a) Healthy retina. (b)retina at risk. (c) Retina with glaucoma.

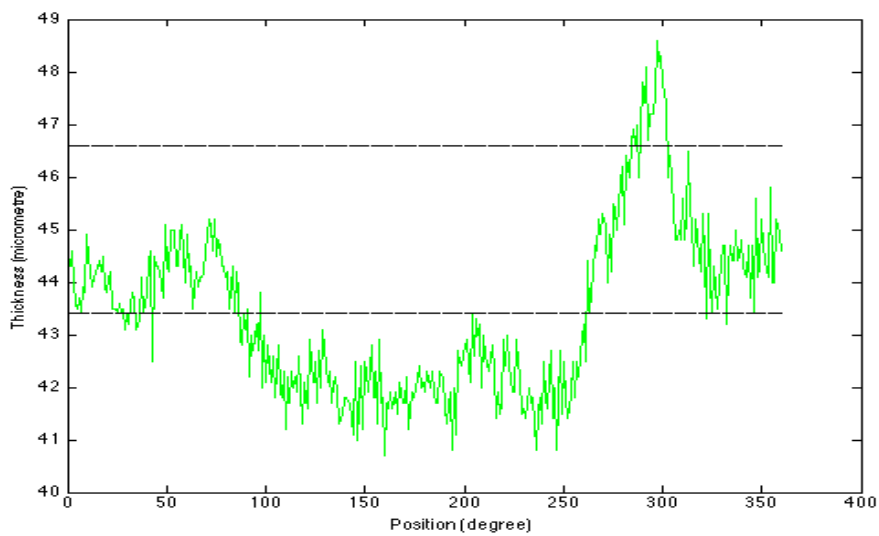
thickness values that fall within the range of 5^{th} – 95^{th} percentile of the normal profile distribution. Any RNFL thickness values within this range are considered healthy eyes.

The red area shows values below 1^{st} percentile of the RNFL thickness of normal distribution. Any RNFL thickness values at this range are considered disease eyes.

The yellow region are values that are below the 5^{th} but above the 1^{th} percentile of normal thickness distribution. Any RNFL thickness values at this range are at risk of developing the



(a)

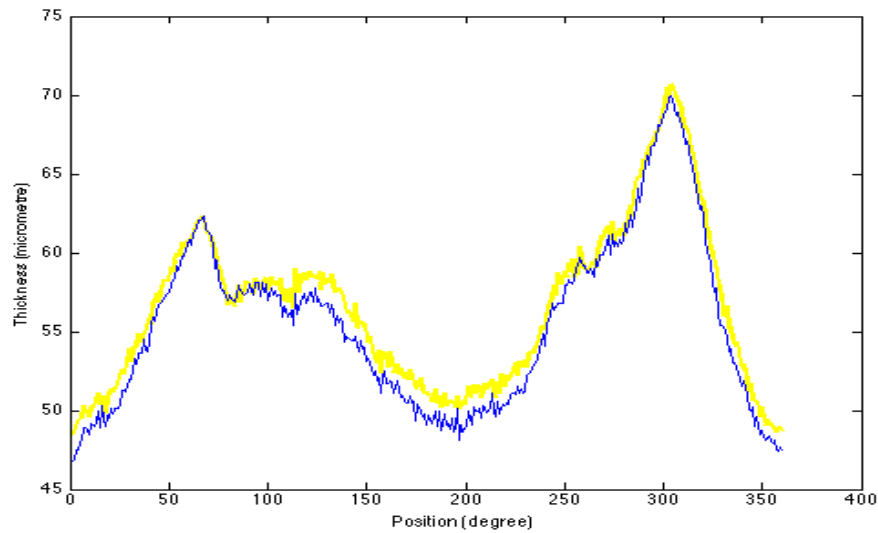


(b)

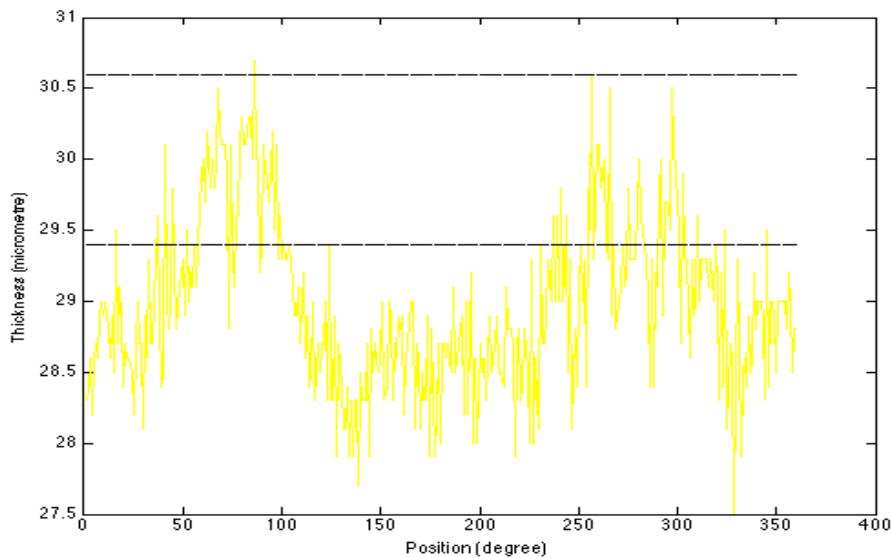
Fig. 11. Results. (a) RNFL thickness profile of healthy retinal images: Green proposed segmentation method. Blue Manual segmentation (b) Error in RNFL thickness profile of healthy retinal images: black lines the standard deviation.

disease (borderline). Figure 10 shows the RNFL thickness profile for healthy retina in green, retina at risk in yellow and in red the glaucoma retina.

In Fig. 11(a), we provided the average thickness profile graph of the proposed method on 100 healthy images in green compared to manually segmented healthy images in blue and Fig. 11(b) shows the profile error of healthy retinal images. The results of this graph show effective agree-



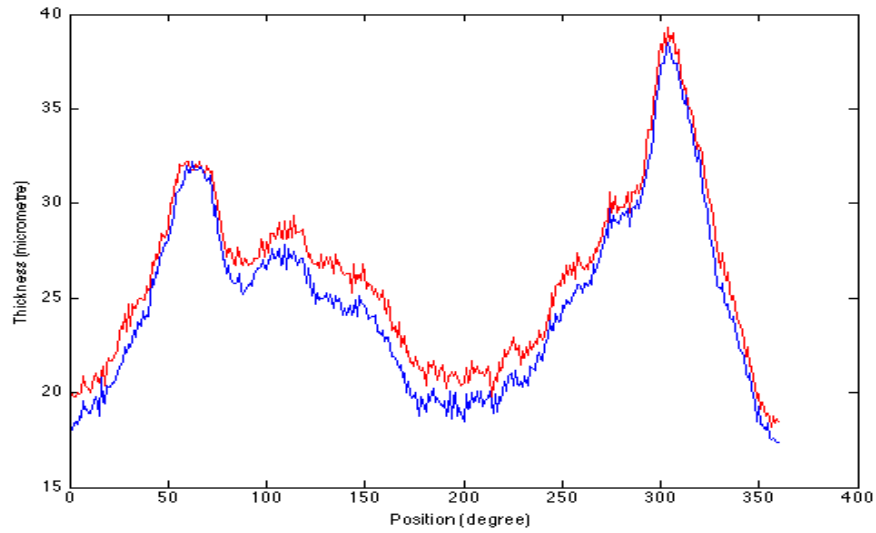
(a)



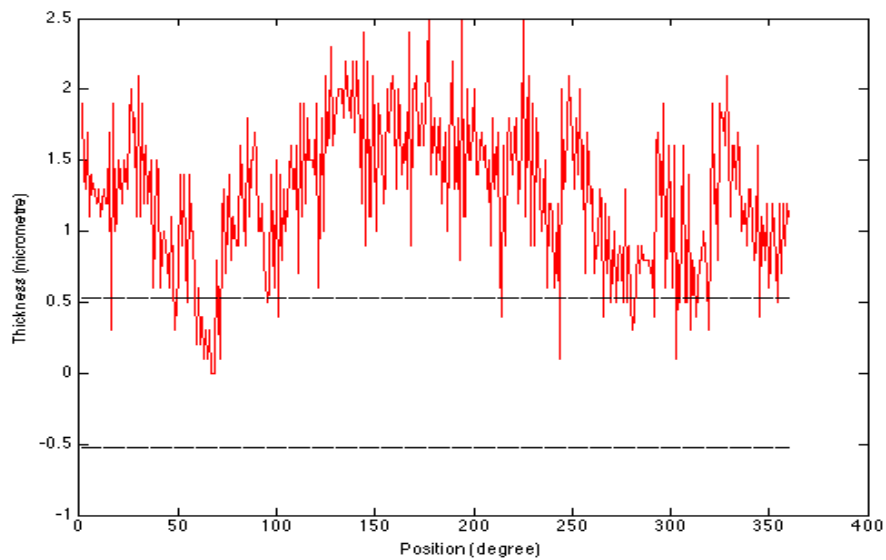
(b)

Fig. 12. Results. (a) RNFL thickness profile of retinal images with risk of glaucoma: Yellow proposed segmentation method. Blue Manual segmentation. (b) Error in RNFL thickness profile of retinal images with risk of glaucoma: black lines the standard deviation.

ment with manual annotations and the normative database as the thickness values of the graph are within the normal limits (green). Figure 12(a) also shows the average thickness profile graph of the proposed method on 10 retinal images with risk of developing glaucoma in yellow and the corresponding manually segmented images in blue. Figure 12(b) shows the corresponding error of the profile representation. Similarly, the results in Fig. 12(a) also demonstrated successful agreement with normative database since the thickness values of the graph are within



(a)



(b)

Fig. 13. Results. (a) RNFL thickness profile of retinal images with glaucoma: red proposed segmentation method. Blue Manual segmentation. (b) Error in RNFL thickness profile of Glaucoma retinal images: red the error. Black lines the standard deviation.

the borderline (yellow). Figure 13(a) shows the average thickness profile graph of the proposed method on 10 glaucoma retinal images in red and the corresponding manually segmented images in blue. The corresponding error profile is shown in red in Fig. 13(b). The results also shows successful agreement with normative database since the thickness values of the graph are within the borderline (red).

4. Conclusions

This study presents an automated approach for retinal layers segmentation by integrating the mechanism of the kernel mapping into the graph cut technique and the polynomial-fitting algorithm. The overall process includes a pre-processing step that enhances the contrast of the retinal layers in the SD-OCT circular scan image around the ONH using a bias correction operation and a segmentation step that includes kernel graph cuts and continuous max-flow algorithms. The method proved to be flexible, accurate, robust and fast, leading to successful segmentation results of the three main retinal layers boundaries used to assess and monitor retinal diseases such as glaucomatous damage. However there are many aspects of this study that can be improved. This includes the removal of blood vessel artefacts in the OCT image without affecting the RNFL thickness measurements and the extension of the proposed method to 3-D OCT image segmentation. The advantage of the 3-D retinal layers segmentation is to use the contextual information in the 3-D structure to improve the segmentation of different layers and also allows the detection of more intra-retinal layers.